Thermal emission from the hot Jupiter WASP-103 b in J and Ks bands

Shi, Y.; Wang, W.; Zhao, G.; Zhai, M.; Chen, G.; Jiang, Z.; ... ; Esteves, L.

Monthly Notices of the ROYAL ASTRONOMICAL SOCIETY

MNRAS **522,** 1491–1503 (2023) https://doi.org/10.1093/mnras/stad891
Advance Access publication 2023 March 28

Thermal emission from the hot Jupiter WASP-103 b in *J* and *Ks* bands

Yaqing Shi,[1,2,3] Wei Wang,[1,3]★ Gang Zhao,[1] Meng Zhai,[1,3]★ Guo Chen,[4] Zewen Jiang,[1,2] Qinglin Ouyang,[2,3] Thomas Henning,[5] Jingkun Zhao,[1] Nicolas Crouzet,[6] Roy van Boekel[5] and Lisa Esteves[6]

[1]*CAS Key Laboratory of Optical Astronomy, National Astronomical Observatories, Chinese Academy of Sciences, Beijing 100101, PR China*
[2]*School of Astronomy and Space Science, University of Chinese Academy of Sciences, Beijing 101408, China*
[3]*Chinese Academy of Sciences South America Center for Astronomy, Chinese Academy of Sciences, Beijing 100012, PR China*
[4]*Key Laboratory of Planetary Sciences, Purple Mountain Observatory, Chinese Academy of Sciences, Nanjing 210023, PR China*
[5]*Max Planck Institute for Astronomy, Königstuhl 17, D-69117 Heidelberg, Germany*
[6]*Leiden Observatory, Leiden University, Postbus 9513, NL-2300 RA Leiden, the Netherlands*

Accepted 2023 March 20. Received 2023 March 20; in original form 2022 October 27

ABSTRACT

Hot Jupiters, particularly those with temperature higher than 2000 K, are the best sample of planets that allow in-depth characterization of their atmospheres. We present here a thermal emission study of the ultrahot Jupiter WASP-103 b observed in two secondary eclipses with CFHT/WIRCam in J and K_s bands. By means of high precision differential photometry, we determine eclipse depths in J and K_s to an accuracy of 220 and 270 ppm, which are combined with the published *HST*/WFC3 and *Spitzer* data to retrieve a joint constraints on the properties of WASP-103 b dayside atmosphere. We find that the atmosphere is best fit with a thermal inversion layer included. The equilibrium chemistry retrieval indicates an enhanced C/O ($1.35^{+0.14}_{-0.17}$) and a supermetallicity with [Fe/H]$= 2.19^{+0.51}_{-0.63}$ composition. Given the near-solar metallicity of WASP-103 of [Fe/H] $= 0.06$, this planet seems to be ∼100 more abundant than its host star. The free chemistry retrieval analysis yields a large abundance of FeH, H^-, CO_2, and CH_4. Additional data of better accuracy from future observations of *JWST* should provide better constraint of the atmospheric properties of WASP-103b.

Key words: techniques: photometric – planets and satellites: atmospheres – planets and satellites: gaseous planets – planets and satellites: individual:(WASP-103b).

1 INTRODUCTION

The recent decades have seen vast progress in the study of the atmospheres of extrasolar planets, thanks to the rapid developments of both observation technique and planet spectral modelling. Transiting exoplanets, especially hot Jupiters (HJs) and ultrahot Jupiters (UHJs), are key objects that provide a wealth of vital information about their atmospheres as well as their systems (Seager & Deming 2010). HJs are gas giant planets that have very short orbital periods with $P <$ 10 d, and probably tidally locked to their parent stars, which have dayside equilibrium temperature $T_{eq} > 1000$ K (Dawson & Johnson 2018). UHJs have shorter orbital periods and receive irradiation 10–100 times the insolation of classice HJs, resulting in the equilibrium temperatures in excess of 2000 K (Baxter et al. 2020). Under such conditions, most molecules including water become partially thermally dissociated and alkalies are mostly ionized (Fortney et al. 2008), leading to one of the most significant differences between HJs and UHJs, i.e. water is common in HJ but is missing in UHJs. Besides, simulations indicate that the dayside hemispheres of UHJs have temperature inversion layers because the absorption of the stellar radiation by species, such as metals, metal hydride, and metal oxides, is strong (Gandhi & Madhusudhan 2019; Lothringer & Barman 2019; Yan et al. 2022). Therefore, HJs and UHJs are expected to be different in their temperature–pressure (T–P) profiles and chemistry regime, and their comparisons should shed constraint on the atmosphere modelling of exoplanets.

Both HJs and UHJs are the most preferable targets for observational studies of planet atmospheres, given their large planet-to-star radius ratio, high T_{eq}, and inflated atmospheres. Observing them at multiple wavelengths allows us to measure the spectral features arising from planetary atmospheres, with which we are able to constrain the temperatures, chemical abundances, and mixing ratios of the atmospheres (Deming & Seager 2009; Madhusudhan et al. 2016). Such studies are mainly carried out based on transmission and emission spectra obtained by spectrophotometric or multiband photometric observations during primary transits and occultations (or secondary eclipses) of HJs.

Transmission spectra are known to preferably probe high-altitude atmospheres and outer atmospheres at the terminator regions. Some planets have clear or not very cloudy atmospheres that allow detection of molecules and atoms including H_2O, alkali metals Na and K (e.g. Deming et al. 2013; Nikolov et al. 2014; Casasayas-Barris et al. 2017), while others may bear high-altitudes clouds/haze and may be too opaque for any spectral features to be detected (e.g. Gibson et al. 2013; Sing et al. 2016; Mackebrandt et al. 2017).

★ E-mail: wangw@nao.cas.cn (WW); mzhai@nao.cas.cn (MZ)

On the other hand, thermal emission spectra are sensitive to the atmospheric temperatures at a range of pressures and heights, and thus can in principal provide constraints on the vertical thermal and chemical profiles of the dayside atmospheres. Such observations have been done on several dozens of planets in the last decade using a wide range of facilities. Theoretical interpretations to these data have led to the discoveries of thermal inversions (e.g. Burrows, Budaj & Hubeny 2008; Knutson 2009; Kreidberg et al. 2018), non-equilibrium chemistry (e.g. Stevenson et al. 2010; Madhusudhan & Seager 2011), and carbon-rich atmospheres (e.g. Madhusudhan et al. 2011a, b). Among them, the *Hubble Space Telescope* (*HST*) plays a crucial role, particularly for the study of water content using the *HST*'s Wide Field Camera 3 (WFC3) G141 grism. Thanks to the high-quality spectra obtained with *HST*, population studies have been performed recently, resulting in major advance towards the understanding of the atmospheres of HJs (cf. Sing et al. 2016; Mansfield et al. 2021). Analysing transmission spectra of 19 exoplanets spans from cool mini-Neptunes to HJs, Welbanks et al. (2019) conducted a homogeneous survey of Na, K, and H_2O abundances and reported a mass-metallicity trend of increasing H_2O abundances with decreasing mass, which provided new constraints on the formation mechanisms of the gas giants. Edwards et al. (2022) suggested that the general lack of trends seen in the transit spectroscopy of the gaseous exoplanets (including WASP-103b) could be either due to the insufficient spectral coverage or the lack of a simple trend across the whole population or the essentially random nature of the target selection. Combining the data of *HST* and *Spitzer*, Changeat et al. (2022) presented an retrieval analysis of 25 HJs and UHJs (including WASP-103b) on emission spectra and claimed an apparent link between the abundance of optical absorbers in their atmospheres and the temperature structures.

Nevertheless, the *HST*/WFC3 data cover the wavelength range from 1.1 to 1.7 μm, where H_2O normally have strong spectral features, while other prominent molecules like CO, CO_2 are relatively weak. The knowledge of CO and CO_2 may help to constrain the atmospheric C/O ratio, which is connected to the question where these planets have formed, when comparing with the C/O ratio of their parent stars. Thus, measurements of thermal emission in other bands are vital for a more completed picture of planet atmospheres, especially when combined with *HST* near-infrared (NIR) data. In addition, extending wavelength coverage, particularly to longer wavelengths, would help to place stringent constraints on the atmospheric thermal profiles of the targeted planets and to detect possible thermal inversion layers (e.g. Madhusudhan et al. 2011b).

WASP-103 b is an UHJ with a mass of ∼1.5 $M_{\rm Jup}$, an inflated radius of ∼1.5 $R_{\rm Jup}$. It orbits a relatively bright ($V = 12.1$, $K = 10.8$) F8V main-sequence star with a short period of ∼22.2 h (Gillon et al. 2014). As a probably tidally locked planet, WASP-103 b may possess an extremely temperature gradient between its two hemispheres. Its brightness temperature on the dayside is estimated to be ∼2500–3200 K, as given by the *Spitzer* measurements of eclipse depths at 3.6 and 4.5 μm (Kreidberg et al. 2018; Pass et al. 2019). A nearby fainter star at an angular separation of 0.242 ± 0.016 arcsec to WASP-103 is detected, which may lead to flux contamination to the unresolved photometric observations (Ngo et al. 2016; Southworth & Evans 2016).

Lendl et al. (2017) detected enhanced absorption of alkali (Na, K) in the transmission spectrum (550–960 μm) of WASP-103b using Gemini/GMOS, however, they could not confirm the previously inferred anomalous slope at bluer optical wavelengths (Southworth et al. 2015; Southworth & Evans 2016). Later, Wilson et al. (2020) presented ground-based VLT/FORS2 observations revealing a featureless transmission spectrum (400–600 μm) with neither alkali metal absorption nor strong scattering slope. However, combined with the additional data from Gemini/GMOS, *HST*/WFC3, and *Spitzer* observations, H_2O absorption was detected at 4.0σ level, suggesting a relatively clear atmosphere in the terminator region. Very recently, Kirk et al. (2021) presented a thorough study based on their new ground-based optical transmission spectrum and archival data of WASP-103b. They detected a downwards slope at bluer wavelengths that was best fit by unocculted faculae, and claimed weak detection of H_2O, HCN, and TiO.

Cartier et al. (2017) using *HST*/WFC3 obtained a featureless emission spectrum in NIR, which suggested the presence of thermal inversion layer or cloud/haze which had muted spectral signals from molecules and atoms. Based on the data obtained by *HST*/WFC3 and *Spitzer*/IRAC, Kreidberg et al. (2018) concluded that the phase-resolved spectra in the WFC3 bandpass are consistent with blackbody emission, while that in the *Spitzer* bands seem to have higher brightness temperature, which is likely caused by CO emission and thermal inversion. Water vapour was recently detected in WASP-103b by Changeat (2022) with depleted abundances of $\sim 10^{-5}$, consistent with the thermal dissociation of this molecule. Re-analysing the same *HST* and *Spitzer* data, Changeat (2022) confirmed the existence of the dayside thermal inversion and attributed it to the thermal dissociation of H_2O, based on the 1D and 1.5D retrievals of the full-phase observations of WASP-103 b. In addition, they determined a solar metallicity with $\log Z = -0.23^{+0.38}_{-0.44}$ and a solar C/O ratio of $0.57^{+0.17}_{-0.23}$.

In this paper, we present a thermal emission study based on our ground-based high-precision eclipse observations of the HJ WASP-103 b in J and $K_{\rm s}$ band with CFHT in 2015 (PI: Wei Wang), and an archival CFHT $K_{\rm s}$ band data taken in 2014 (PI. Delrez). Details of the observations are described in Section 2, following by introduction of data reduction and analysis in Section 3. We compare the observations to model spectra in Section 4 and summarize our discussion in Section 5.

2 OBSERVATIONS AND DATA REDUCTION

We observed two secondary eclipses of WASP-103 b with the Widefield InfraRed Camera (WIRCam; Puget et al. 2004) on the Canada–France–Hawaii Telescope (CFHT). WIRCam has a large field of view (FOV) of 21 arcmin × 21 arcmin, which allows to cover a large number of appropriate reference stars for differential photometry. The two observations were taken respectively in the J band on 2015 June 9, and in the $K_{\rm s}$ band on 2015 May 28. The total observation time for each run is ∼5.5 h, covering the entire eclipse assuming a circular orbit, and ∼2.5 h out-of-eclipse observations. The airmass ranges from 1.02 to 1.37 and 1.02 to 2.01 for the J and Ks band, respectively. The night of June 9 was photometric with a median seeing of 0.88 arcsec, however, the May 28 night was not ideal bearing large sky variations. The atmospheric extinctions of two observations are reported to be ∼0.06 mag. As described in Section 3.3, we also employed the $K_{\rm s}$-band data taken on 2014 May 20 from 06:50 to 12:40 UT (Program ID: 14AO38, PI: L. Delrez) with a very similar observation strategy. For more details, please refer to section 3.1 in Delrez et al. (2018).

In order to achieve ultrahigh photometric precision down to $\sim 10^{-4}$ as required by our science goals, the 'Staring Mode' (Devost et al. 2010) was adopted in both observations, following previous successful experiments (e.g. Croll et al. 2010a, b; Wang et al. 2013). The Staring Mode is designed to keep the pointing of the telescope as stable as possible, so that the effect of intrapixel and interpixel

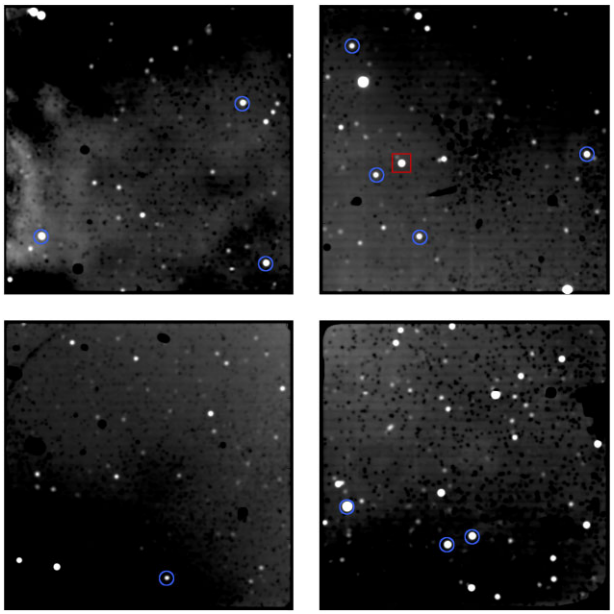

Figure 1. CFHT/WIRCam full-frame reduced image during our observation of WASP-103 b in the *J* band. WASP-103b is marked with a red square and the final 11 reference stars that were used are marked as blue circles.

variations of detectors on photometric precision could be largely weakened.

The full WIRCam array is used to include reference stars as many as possible. The telescope was defocused to 1.7 and 1.8 mm for *J*- and K_s-band observations, resulting in a donut-shaped PSF with a radius of ∼4 arcsec. This is to further minimize the impact of flat-fielding uncertainties and intrapixel sensitivity variations, as well as to keep the flux of the target and reference stars well below the detector saturation level with reasonably long exposure time and thus low fraction of overhead. We applied a detector integration time (DIT) of 10 and 15 s for *J* and K_s bands, respectively, and NDIT = 12. The overall duty is 39.8 per cent for K_s-band run, and is 50.3 per cent for *J*-band run. Fig. 1 is a full-frame reduced image showing the observing FOV, with the target star and the final selected reference stars marked as black squares and red circles, respectively. Given that WASP-103 is bright, and the exposure times and defocus amounts that were set for our run for the purpose of minimizing systematics, the number of available reference stars in the FOV is limited. This results in relatively large observation uncertainties as compared to theoretical predictions from Devost et al. (2010).

The raw data were reduced using the ′I′iwi pipeline version 2.1.200[1], including flagging the saturated pixels, non-linearity correction, reference pixels and dark subtraction, flat-fielding, bad pixels, and guide window masking. The ′I′iwi pipeline construct bad pixel masks from darks and dome flats. The bad pixel mask has 1 for good pixels and the float Not-a-Number (NaN) value for bad pixels. There might be bad pixels within the photometry aperture of the target and reference stars. In order to improve the accuracy and the signal-to-noise ratio, these bad pixels were flagged, and their values were replaced by interpolating the counts of their adjacent pixels. Aperture photometry was then performed on the reduced image for the target star and dozens of candidate reference stars that were not

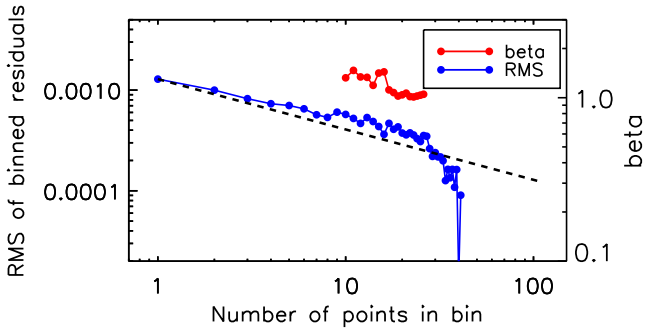

Figure 2. RMS and noise factor β of our residuals to the best-fitting model for the various data sets in *J* band.

used as guiding stars. Fractional contribution of pixels at the edge of the circular aperture were taken into account. Stars of similar brightness with ($\Delta m < 2.5$ mag) in the FOV, particularly those in the same WIRCam chip, were selected as candidate reference stars. We kicked out the reference stars whose out-of-eclipse light curves are quite different from others, or possess relatively large photometric variation. For each star, 11 different aperture radii were applied with a step of 0.5 pixels. The final aperture radii and the final selection of reference stars will be determined in the iteration procedures of finding the best-fitting light curves, as described in detail in the following sections.

3 DATA ANALYSIS AND RESULTS

3.1 Light-curve derivation and modelling

We start from the technique presented by Everett & Howell (2001) to obtain high-precision differential light curves with various aperture sizes and different combinations of reference stars. First, for each aperture diameter *D* and each reference star, each raw light curve is normalized individually with their median values determined by 2σ–3σ clipping algorithm. Then, an average reference light curve at a *D* and a reference star group (RSG), $L_{\mathrm{ref(D,\,RSG)}}$, is obtained by taking the weighted averages of each normalized light curve, with the weights being the inverse of photometric errors. Then, the average reference light curve is employed to differentiate the target light curve to remove systematics. A 5σ cut is applied to remove obvious outliers in the normalized target light curve. Besides, there is an obvious time-correlated trend in the normalized observed light curve, which is referred as the background trend and could be roughly modelled as a linear function, defined by the out-of-eclipse light curve with time:

$$B_f = c_1 + c_2 t, \tag{1}$$

where c_1, c_2 are fitting parameters, t is time relative to the middle eclipse time in the unit of seconds.

The target light curves are then modelled using the IDL package EXOFAST[2] (Eastman, Gaudi & Agol 2013). This suite of routine uses Markov chain Monte Carlo (MCMC) methods to fit the model to Mandel & Agol (2002) observations (Ford 2005). Background baseline trend has been observed in almost all previous NIR eclipse light curves (Croll et al. 2010a, b; Wang et al. 2013; Delrez et al. 2018), which probably originate from the variations in instruments and/or atmospheric conditions and should be removed or modelled to

[1]https://www.cfht.hawaii.edu/Instruments/Imaging/WIRCam/IiwiVersion2Doc.html

[2]https://exoplanetarchive.ipac.caltech.edu/docs/exofast/exofast_home.html

reveal the planet signal. In this work, B_f is first detrended with a linear function of t to the out-of-eclipse part light curve. The remaining baseline is then fit jointly with a polynomial function and the eclipse model, to avoid possible overfitting using EXOFAST. The polynomial function we used is dependent on the time relative to the eclipse centre in seconds t, the image coordinates of the target star x and y in pixels, and the width w in pixels of the target's point spread function (PSF), as described in equation (2).

To evaluate the amount of correlated noise in each light curve $L_{\mathrm{ref(D,\,RSG)}}$, the best-fitting model data residuals are binned down to be compared with the expected Gaussian noise of one over the square root of the bin size (Fig. 2). To quantify the amount of correlated noise in our data sets, the parameter β defined by Winn et al. (2008) is used, which is the ratio of the residuals to the Gaussian noise expectation (see Fig. 2). To determine β, we calculate the average ratios with bin sizes of 15–85 data points, as shown in red in Fig. 2. It sometimes occurs oddly that the scaled-down residuals are smaller than the Gaussian noise expectation, i.e. $\beta < 1$. For such cases, we set $\beta = 1$.

3.2 Optimal techniques to determine the 'best' light curves

It is realized that for almost each combination of D and RSG, an eclipse-like light curve could be found with different measured eclipse depths, errors, and best-fitting residuals. This fact, on one hand, assures that our data do detect thermal emission from the target planet. While on the other hand, this calls the requirement for a further step to find the 'best' combination of D and RSG, which produce the 'best' light curve that could be fitted by an eclipse light-curve model with the smallest residuals, while no hint for overfitting is noticeable.

For the case of D small but still large enough to contain most stellar photons, the rms of residuals of the light curve with best-fitting model subtracted is small, as the impact of sky background is mitigated at small D. While for large D, the vast majority of the light from stars are included in aperture photometry even during moments of poor seeing and guiding, thus red noise could be best fit and removed, resulting $\beta \sim 1$. Therefore, we use rms and β as proxies to achieve a balance between the two competing factors: avoiding high sky background that arises from with large D, and reducing the presence of time-correlated noise that comes along with small D. In this work, we explore all the combinations RSG and various values of D to seek the minimum value of the metric rms$\times$ β^2, following by the prescription of Croll et al. (2015). Fig. 3 shows an example on how to determine the best combination of D and RSG.

3.3 Light-curve fitting

Following the methods described above, light curves $L_{\mathrm{ref(D,\,RSG)}}$ are obtained for various combinations of aperture size D and RSG, and the best combination of D and RSG is found by finding the minimum value of rms$\times$ β^2. As shown in Fig. 3, for J-band data, choosing $D = 34$ and including the best five reference stars yield the best-fitting results. In this step, the same D is used for the target and reference stars. After the best combination of D and RSG is found, we further look for the best light curve by varying individually D of each reference stars with a step of ± 1 pixel. The best-fitting light curve is shown in Fig. 4, for which an eclipse depth of 1170 ± 190 is derived. The resulting D of each reference star is slightly different from the same-D fitting result. There are about $\sim$3–5 data points exceeding 5 times the standard deviation of the corrected target light curve, which are marked as outliers and are removed from model fitting.

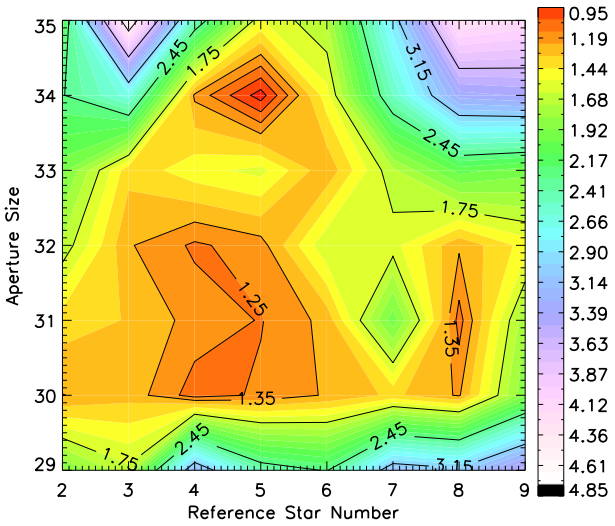

Figure 3. The normalized rms$\times$ β^2 distribution overlaid with contour maps for the various combinations of aperture diameter D and the number of reference star group (N_{RSG}) in the J band. The minimum value of rms$\times$ β^2 is reached with $D = 34$ and $N_{\mathrm{RSG}} = 5$.

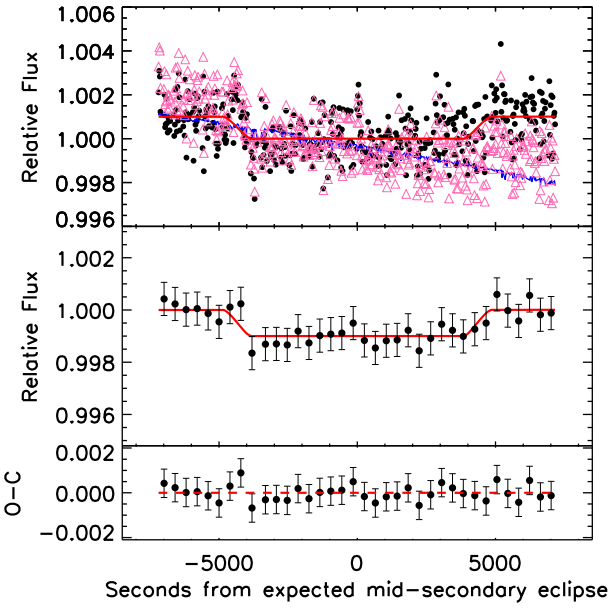

Figure 4. The secondary eclipse of WASP-103b observed by CFHT/WIRCam in J band on 2015 June 9. The top panel shows the unbinned light curve with the polynomial function fitting of the red noise (blue line) and the unbinned light curve subtracted red noise with the best-fitting secondary eclipse model (red line). The second panel shows the binned light curve divided by the best-fitting model (red line). Bottom panel shows the binned residuals from the best-fitting model. The rms of the binned residuals is 654 ppm (7.8min bins). The contamination from the nearby star is not corrected here.

Assuming a circular orbit, we produced the J-band secondary eclipse light-curve model by setting SECONDARY and SPECPRIORS keywords of EXOFAST and used the latest published parameters as priors. For the implementation of the secondary eclipse case, we enforced the limb darkening coefficients to be zero. Our model

includes 12 prior parameters in total. A de-correlatively polynomial function was applied in order to fit the baseline curve, with the function:

$$f = 1 + a_1 x + a_2 x^2 + a_3 y + a_4 y^2 + a_5 t + a_6 t^2 + a_7 r + a_8 r^2, \quad (2)$$

where $a_{1,\,2...8}$ are the coefficients to be derive, x, y are the positions of the centroid of the target star, t is the time relative to the eclipse centre in seconds, and r is the stellar PSF full width at half-maximum (FWHM). We run 10^6 steps in the MCMC chain, yielding best-fitting results as listed in the second column of Table 1 and the posterior distribution plots are shown in Fig. A1.

Due to the bad observable conditions in 2015 May 28, the data set obtained for K_s band does not meet the precision requirement for our scientific goal. Therefore, we employed the data taken on 2014 May 20 from 06:50 to 12:40 UT (Program ID: 14AO38, PI: L. Delrez), with a very similar observation strategy, to determine the K_s eclipse depths. For details of this data, please refer to Delrez et al. (2018). We note that the 2014 K_s-band observation has an FOV slightly different from that of the J-band observation, thus a new RSG and D are to be found. The data then were reduced and analysed in the same manner as described above for the J-band data. As a result, shown in Fig. 5, choosing $D_{\mathrm{ref_i}} = 36$ and 3 reference stars yield an initial best-fitting result. Similarly, we applied a 3σ threshold to remove the outlying data points to obtain a 'cleaner' target light curve, with which we obtained the best differential light curve in K_s, as presented in Fig. 6. The derived parameters are listed in the third column of Table 1.

We note that the data points at the beginning of each observation have a relatively large systematic error, therefore we only used the data with $T - T_{\mathrm{mid}}$ between -8500 and 8500 s when performing light-curve fitting and eclipse depth determination. It is also notable that our measurement of the K_s-band secondary eclipse depth is quite different ($>5\sigma$) from those reported by Delrez et al. (2018), which might be caused by different baseline continuum shapes that may have a different impact on the quadratic terms of baseline fitting. Note that their derived eclipse depth is higher than their model predictions (cf. fig. 5 in their paper).

3.4 Flux decontamination and eclipse depths

The 'measured' eclipse depth from the unresolved photometric light curve may be underestimated if a nearby companion is included in the aperture. Therefore, flux contamination from nearby companions must be corrected before determining the planet-to-star flux ratio F_P/F_S. WASP-103 was reported to have a close companion, that may dilute the measurements of its eclipse depths. Wöllert & Brandner (2015) found that the companion is 0.242 ± 0.016 arcsec from their i- and z-and observations. Ngo et al. (2016) provided further evidence in *JHKs* with the measured magnitudes difference of $\Delta J = 2.427 \pm 0.030$, $\Delta H = 2.2165 \pm 0.0098$, and $\Delta Ks = 1.965 \pm 0.019$. They claimed that the companion might be bounded to WASP-103. This conclusion was later confirmed by Cartier et al. (2017), but was questioned by a more recent work by Barros et al. (2022), as indicated by a non-detection of the visual companion via lucky imaging observations and the RV observations with CORALIE. Whether the fainter star is bounded to WASP-103 or not, at such a small angular separation, it would anyway contaminate the flux measurements in both transmission and emission spectra.

The flux contamination ratio is simply the ratio of the flux of the contaminant to that of the target star, i.e. $F_{\mathrm{con}}/F_{\mathrm{W103}}$ in our case. Their values are listed in Table 2, which can be directly calculated using the observed magnitude differences $\Delta J = 2.427 \pm 0.030$ and $\Delta K_s = 1.965 \pm 0.019$ from Ngo et al. (2016). Then, F_P/F_S is given by

$$\frac{F_P}{F_S} = \mathrm{d}_\lambda \times (1 - \frac{F_{\mathrm{con}}}{F_{\mathrm{W103}}})^{-1}, \quad (3)$$

where d_λ is the 'measured' eclipse depth before flux decontamination correction at the central wavelength λ of each passband.

The decontaminated secondary eclipse depth we obtained for J band in this work is 1310 ± 220, well consistent with Cartier et al. (2016) and Kreidberg et al. (2018), which obtained an eclipse depth of 1256^{+154}_{-155} ppm at $\lambda \sim 1.252\mu$m and 1480 ± 46 ppm at $\lambda \sim 1.275\mu$m, respectively. Note that the eclipse depth from Cartier et al. (2016) is $\sim$10 per cent lower than that from Kreidberg et al. (2018), which is likely a result that the latter analysis considers the planetary thermal phase variation, at an order of $\sim$100 ppm. If we take the amplitude of the effect into account, our result for the J band is only $\sim$40 ppm smaller than that of Kreidberg et al. (2018). Applying a simple linear interpolation, we calculate the result for K_s band. However, the amplitude-correct results could not fit the model well, thus, we utilize the uncorrected results in atmospheric model fitting.

4 THE ATMOSPHERIC PROPERTIES OF WASP-103B

4.1 Atmospheric modelling

Fig. 7 shows the dayside emission spectra of WASP103 b to be investigated in this work, including the photometric eclipse depths derived from the ground-based J and K_s observations (purple square), those from *Spitzer* observations (Kreidberg et al. 2018), and those from *HST* (black filled circles Cartier et al. 2016). As reported by several previous work (Cartier et al. 2016; Kreidberg et al. 2018), WASP-103b seems to be featureless in the *HST*/WFC3 band, except for the very recent work by Changeat (2022), which reported detection of H-, H_2O, CO, and CH_4. Therefore, adding K_s-band data may provide crucial information to constrain the planet's atmosphere, particularly the C abundance and the carbon-to-oxygen (C/O) ratio. It is quite interesting that the last *HST* data point and our K_s data are significantly lower than the J-band data and the other *HST* data points, which should be related to the opacity of CO_2 and/or CO molecules.

We follow the exoplanetary atmospheric modelling and retrieval technique of Madhusudhan & Seager (2009) to investigate the dayside atmosphere of this planet. The spectral retrieval analyses are performed using the open-source package `petitRADTRANS` (Mollière et al. 2019). We assume a 1D parallel atmosphere with 100 layers, divided equally in logarithmic space from 10^3 to 10^{-6} Pa, and the `PyMultiNest` (Buchner et al. 2014) code to calculate the Bayesian evidence, which represent the average likelihood under the prior for a specific model choice. `PyMultiNest` implements the multimodal nested sampling algorithm based on the `MultiNest` library (Feroz, Hobson & Bridges 2009).

As pointed out by previous works, WASP-103 b seems to possess a dayside thermal inversion layer (Delrez et al. 2018; Kreidberg et al. 2018; Changeat 2022). Therefore, we adopt a two-point T–P profile (Brogi et al. 2014) that allows thermal inversion, which assumes an isothermal atmosphere at altitudes above the lower pressure point (T_1, P_1) and below the higher pressure point (T_2, P_2), while T changes linearly with $\log P$ between the two points. T ranges between 0 and 4000 K. The retrieved T–P profiles are shown in Fig. 7, implying the presence of thermal inversion in the atmosphere of WASP-103 b.

We consider two different models with either free chemistry (hereafter the FREE model) or equilibrium chemistry (hereafter

Table 1. Best-fitting secondary eclipse parameters in J and K_s bands.

Parameter	J	K_s
Stellar parameters		
M_* ($M_\odot$)	$1.223^{+0.085}_{-0.080}$	$1.225^{+0.085}_{-0.082}$
R_* ($R_\odot$)	$1.433^{+0.033}_{-0.032}$	1.434 ± 0.033
L_* ($L_\odot$)	$2.59^{+0.46}_{-0.40}$	$2.58^{+0.45}_{-0.41}$
$\log g_*$ (cgs)	$4.2129^{+0.0099}_{-0.010}$	$4.2131^{+0.0099}_{-0.010}$
$T_{\rm eff}$ (K)	6110 ± 200	6120 ± 200
[Fe/H] (dex)	0.06 ± 0.13	0.06 ± 0.13
Planet parameters		
P (d)	$0.925541^{+0.000019}_{-0.000020}$	0.925542 ± 0.000019
a (au)	$0.01987^{+0.00045}_{-0.00044}$	$0.01988^{+0.00045}_{-0.00046}$
$R_{\rm P}$ ($R_{\rm Jup}$)	$1.524^{+0.045}_{-0.044}$	$1.525^{+0.046}_{-0.045}$
T_{eq} (K)	2505 ± 83	2504^{+82}_{-83}
$R_{\rm P}/R_*$	0.1094 ± 0.0020	0.1094 ± 0.0020
a/R_*	$2.9822^{+0.0068}_{-0.0069}$	2.9823 ± 0.0067
Secondary eclipse parameters		
$T_{\rm mid}$ ($BJD_{\rm TDB}$)	$57182.40589^{+0.00023}_{-0.00022}$	56797.38610 ± 0.00023
b (R_*)	$0.0731^{+0.0060}_{-0.0061}$	0.0729 ± 0.0060
T_{12} (d)	0.01150 ± 0.00021	0.01150 ± 0.00021
T_{14} (d)	0.11207 ± 0.00035	0.11208 ± 0.00035
$F_{\rm p}/F_*^a$	0.00117 ± 0.00019	0.00113 ± 0.00023

Note. [a]The derived eclipse depths listed here are not yet corrected for the dilution by the nearby star.

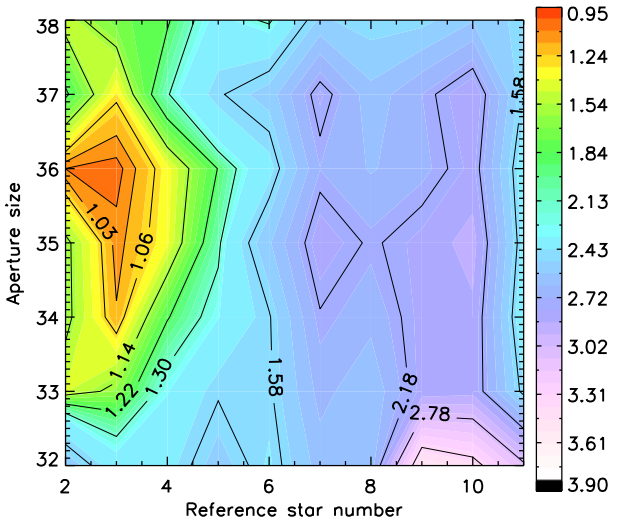

Figure 5. Same as Fig. 3 but for the K_s band. The minimum value of rms$\times \beta^2$ is reached at $D = 36$ and $N_{\rm RSG} = 3$.

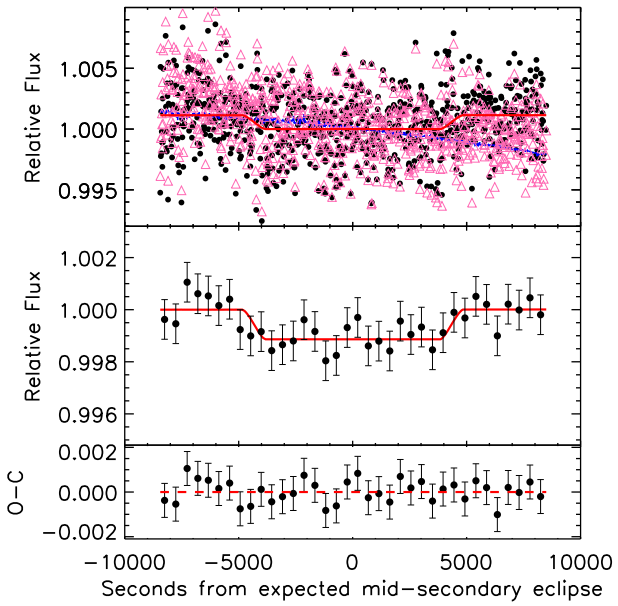

Figure 6. Secondary eclipse light curve of WASP-103 b in K_s band. Same as Fig. 4. The binned residual rms is 775 ppm (8 min bins).

the EQ model). We are aware that assuming equilibrium chemistry is often oversimplified and may not accurately reflect the actual chemical processes occurring in the atmosphere. Moreover, it cannot typically account for the formation of clouds, which could have a significant impact on the temperature and composition of the atmosphere. However, the EQ model is still useful to be served as a starting point for initializing abundances in HJ's atmospheres and for the compaison study with the FREE model results.

For the EQ model case, only two free parameters, i.e. the C/O number ratio and the metallicity [Fe/H] are to be retrieved. As described in Mollière et al. (2017), the mass fraction of each species can be interpolated from a chemical table as a function of P, T, [Fe/H], and C/O. The list of reactant species includes H_2 (Rothman et al. 2013), He (Chan & Dalgarno 1965), CO (Rothman et al. 2010), H_2O, HCN (Harris et al. 2006), C_2H_2, CH_4 (Yurchenko & Tennyson 2014), PH_3 (Sousa-Silva et al. 2015), CO_2, NH_3 (Yurchenko, Barber & Tennyson 2011), H_2S, VO (Mollière et al. 2019), TiO (McKemmish et al. 2019), Na (Piskunov et al. 1995), K, SiO (Barton, Yurchenko & Tennyson 2013), e^- (Gray 2021), H^-, H, and FeH (Wende et al. 2010). The abundance grid is calculated using the package `easyCHEM` (Baudino et al. 2017). The grid dimensions include $T \in [60, 4000]$ K, $\log P \in [$

Table 2. The 'measured' original eclipse depths, the flux contamination ratios, and the decontaminated eclipse depths in J and K_s for WASP-103 b in this work.

Filter	Uncorrected eclipse depths	F_{cont}/F_{W103}	Corrected eclipse depths
J	0.00117 ± 0.00019	0.1070 ± 0.0029	0.00131 ± 0.00022
K_s	0.00113 ± 0.00023	0.1637 ± 0.0029	0.00135 ± 0.00027

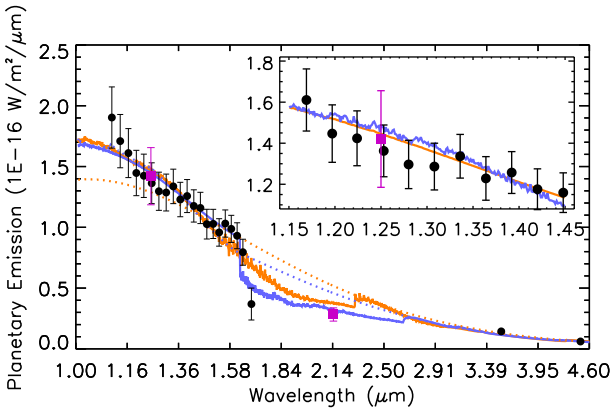

Figure 7. Observations and model spectra of dayside thermal emission of WASP-103b. Our J and K_s data are presented by purple solid square, and other archival data are presented by black solid circle. The orange line shows the EQ model, while the violet line shows the FREE model. The two dotted lines show the EQ and FREE models assuming isothermal.

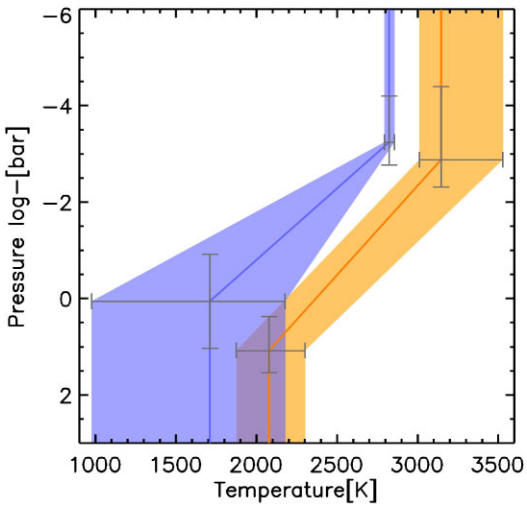

Figure 8. The retrieved vertical T–P profiles for the EQ model (orange) and FREE model (violet) with 1σ confidence intervals, respectively.

$-8, 3]$ bar, C/O $\in [0.1, 1.6]$, and [Fe/H] $\in [-2, 3]$, with 100, 100, 20, and 40 equidistant points, respectively. The sampling sizes are thus $\sim$40 K, $10^{0.11}$ bar, 0.125 dex, and 0.075 for T, P, [Fe/H], and C/O, respectively. The C/O ratio varies with the oxygen abundance, once [Fe/H] is set. It is found that the interpolation with a T sampling grid of 100 K is reasonably accurate to an error budget of a few per cent (e.g. $\sim$1.64 per cent for water, Barton et al. 2017), which is less than the estimated uncertainty in the *ab initio* line lists (Al-Refaie et al. 2021). Given its robustness and rapidness, this approach is widely used in the retrieval analysis of exoplanet atmosphere, although caution should be taken for the atmospheres with one or more of the T-P-[Fe/H]-C/O values out of the preset boundaries.

For the retrievals, only the absorption of H_2O, CO, CH_4, CO_2, TiO, VO, and FeH are included. Logarithmic uniform prior that vary between -10 and 0 are used for each parameter of interest. Collision-induced absorptions (CIAs) of H_2-H_2 and H_2-He (Borysow, Frommhold & Birnbaum 1988; Borysow, Frommhold & Moraldi 1989; Borysow, Jorgensen & Fu 2001; Borysow 2002), bound–free and free–free opacity of H^-, and Rayleigh scattering of H_2 and He are also taken into account (Dalgarno & Williams 1962). For the FREE model, the mass fractions of each species of investigation, instead of [Fe/H] and C/O, vary independently within the given distributions and boundaries. The same molecules as in the case of equilibrium chemistry are included for retrieval. H_2 and He are regarded as filling gases with their mass ratios fixed at the solar values. In addition to the parameters mentioned above, the planet gravity is fixed at 15.8 m s^{-2} and radius at 1.646 R_{Jup} using the literature values from Southworth et al. (2015).

Notable offsets in transit depths measured from the ground-based optical data and the space-based NIR data were reported previously in Alexoudi et al. (2018), Murgas et al. (2020), and Yip et al. (2021) at the orders of 10^{2-3} ppm. In our case, the measured J-band eclipse depth is very close to the *HST* depth at 1.25 μm with only 4 per cent discrepancy, suggesting that the above-mentioned offset between the ground-based optical depth and space NIR depth seems to be minor (at least if in the same band) in this work. Nevertheless, we still perform vertical offset retrievals to find the most appropriate offset in the range of $[-300, +300]$ ppm. Comparing the Bayesian evidence $\ln \mathcal{Z}$ and Bayes factor, we find that the *HST* data with an offset of -200 ppm could provide the best-fitting EQ model, and the *HST* data an offset of -50 ppm was the best for FREE model. These offsets are smaller or comparable to the measurement uncertainties of the eclipse depths. The yielded abundances for the offset-applied cases are shown in Table 3, which are well consistent with the un-offsetted ones within $\leqq 0.2\sigma$. Therefore, we conclude that applying an offset to the *HST* NIR data or not does not change the results and conclusions of this work.

Overall, both retrievals are well consistent with the data, as presented in Fig. 8. The retrieved parameters considered in both equilibrium chemistry and free chemistry models, as well as the χ^2_ν and Bayesian evidence for each retrieval are given in Table 3. The retrieved corner plots are shown in Figs A2 and A3. Note that χ^2_ν of the FREE model is slightly smaller than 1, indicating possible overestimates of the data error.

4.2 Results and discussion

The best-fitting EQ model is shown in Fig. 7 as the yellow line with $\chi^2_\nu = 1.183$ comparing in general well with the observation. Nevertheless, the several reddest *HST* data points and our K_s data stand apart from the model prediction by $\gtrsim 1\sigma$. As listed in Table 3, the best-fitting [Fe/H] and C/O ratio are $2.19^{+0.51}_{-0.63}$ dex and $1.35^{+0.14}_{-0.17}$, respectively, indicating a metal-rich and carbon-rich atmosphere. The significantly high metallicity and C/O ratio in the atmosphere of WASP103 b result in large accumulation of FeH and CO. Given that FeH has strong blue-slope features in the J-band regime, and

Table 3. The fixed and retrieved parameters, χ^2_v and Bayesian evidence for each retrieval.

Parameters	EQ[a]	os = −200[b]	FREE[a]	os = −50[c]
R_p (R_{jup})		1.646 (fixed)		
log g_p (cgs)		3.198 (fixed)		
T_1 (K)	3146^{+384}_{-135}	3384^{+305}_{-318}	2823^{+33}_{-30}	2788^{+36}_{-34}
T_2 (K)	2078^{+224}_{-203}	2178^{+234}_{-252}	1713^{+465}_{-734}	1250^{+719}_{-732}
log P_1 (bar)	$-2.88^{+0.57}_{-1.52}$	$-4.4^{+1.41}_{-1.09}$	$-3.23^{+0.47}_{-0.97}$	$-2.71^{+0.32}_{-1.22}$
log P_2 (bar)	$1.08^{+0.46}_{-0.71}$	$0.87^{+0.76}_{-0.99}$	$0.05^{+0.98}_{-0.98}$	$-0.18^{+1.32}_{-1.15}$
[Fe/H]	$2.19^{+0.51}_{-0.63}$	$2.01^{+0.63}_{-0.89}$		
C/O	$1.35^{+0.14}_{-0.17}$	$1.28^{+0.21}_{-0.24}$	0.86[d]	
$\log_{10}(H^-)$			$-3.72^{+0.29}_{-1.23}$	$-3.58^{+0.24}_{-0.64}$
$\log_{10}(CO_2)$			$-2.66^{+0.92}_{-1.31}$	$-3.89^{+2.06}_{-3.67}$
$\log_{10}(H_2O)$			$-6.05^{+2.24}_{-1.96}$	$-5.94^{+2.40}_{-2.50}$
$\log_{10}$(FeH)			$-3.65^{+1.71}_{-3.38}$	$-4.54^{+2.42}_{-3.40}$
$\log_{10}$(CO)			$-4.55^{+2.60}_{-2.99}$	$-4.80^{+3.15}_{-3.23}$
$\log_{10}(CH_4)$			$-3.24^{+1.56}_{-3.16}$	$-4.94^{+2.99}_{-3.13}$
$\log_{10}$(TiO)			$-5.93^{+2.20}_{-2.16}$	$-6.17^{+2.40}_{-2.38}$
$\log_{10}$(VO)			$-5.13^{+1.78}_{-2.43}$	$-5.63^{+2.31}_{-2.65}$
χ^2_v	1.183	1.756	0.9199	1.348
ln $\mathcal{Z}$	971.9 ± 0.4	972.5 ± 0.0	970.1 ± 1.0	972.7 ± 0.5

Notes. [a]The degrees of freedom (D.o.F) for the EQ and FREE retrievals are 6 and 12, respectively.
[b]The EQ retrieval after applying an offset of −200 ppm to the *HST* data.
[c]The FREE retrieval after applying an offset of −50 ppm to the *HST* data.
[d]This is a rough estimate.

CO has a strong blue-slope emission band from ∼ 2.26 to 3 μm (cf. Fig. 9), their combined emissivity contribution compensates a bit for the relative low emission at 1.62 μm and the K_s band, although still not good enough. This implies that the equilibrium chemistry assumption may not apply to the dayside atmosphere of WASP103 b, as found for many other planets (Kawashima & Min 2021; Roudier et al. 2021; McGruder et al. 2022; Mansfield et al. 2022).

Indeed, as shown in Fig. 8 as the blue line, the FREE model spectrum fits the observation better than the EQ model does, with $\chi^2_v = 0.92$. The best-fitting mass fractions are listed in the third column of Table 3. The most abundant molecules are CO_2, CH_4, FeH, and H^-, which have mass fractions larger than 10^{-4}. Taking into account them and CO, we find a C/O number ratio of 0.86, higher than the solar value, although not as extreme as the EQ model result. Looking into the Fig. 9(a), the overabundance of H^- and the discontinuity at ∼ 1.6 μm seem to be the main reason to account for the sudden decrease of the reddest *HST* data and our K_s data. It is usually the case for classic HJs that H_2O, H^-, and hydrides/oxides (TiO, VO, and FeH) are the major species that contribute to the opacity over the *HST*/WFC3 wavelength range. For WASP103 b, however, the dayside temperature ($T > 1710$ K) is so high that H_2O is dissociated, and H atoms in the higher altitude bond with free electrons and become H^-, which devotes opacity to the atmosphere bringing a continuum absorption (John 1988) and drags down suddenly the spectrum at ∼1.6 μm, as presented in Fig. 8. CO_2 emission is visible near the wavelength of 2.3 and 4.5 μm, yielding a mixing ratio of CO_2 of $-2.66^{+0.92}_{-1.31}$.

In order to verify the reliability of the detected molecules, we follow the approach introduced in Benneke & Seager (2013) and Kreidberg et al. (2022). We remove one molecule at a time and redo the retrieval, and calculate for each model the Bayesian evidence $\mathcal{Z}$, which are listed in Table 4. By comparing $\mathcal{Z}$ between the full model and the model without a given species, we could investigate whether the observation favours the model including that species. The Bayes factor (Kass & Raftery 1995) of CO_2, H^-, CH_4, FeH, and TiO are large enough (>6), indicating that these molecules are largely favoured by the data to be included in the model. As CO does not have strong features in the observed wavelength coverage, the retrieval analysis with CO excluded is similar to the full model.

It is worthy to mention that for each model we investigate in this work, EQ or FREE, or with a certain molecule removed, the retrieved T–P profile possess a thermal inversion layer. This is in hand with the findings in Cartier et al. (2016), Kreidberg et al. (2018), and Changeat (2022). For the atmospheric composition, Cartier et al. (2016) claimed a solar metallicity with C/O>1, while Kreidberg et al. (2018) derived a moderately enhanced metallicity ($23^{+29}_{-13}\times$ solar) and a C/O ratio of 0.9, consistent with our results. Our EQ model yields a [Fe/H] $= 2.19^{+0.51}_{-0.63}$ dex and C/O ratio of $1.35^{+0.14}_{-0.17}$. The FREE model does not set [Fe/H] or C/O as retrieved parameters, and thus cannot place direct constraint on these two parameters. However, we estimate a C/O number ratio of ∼0.96 from the mass abundance of the most dominate species, which is close to the value obtained by Kreidberg et al. (2018). Interestingly, Changeat (2022) used the same *HST* and *Spitzer* data, and yielded a solar metallicity, and a supersolar C/O ratio. Therefore, although whether the atmosphere of WASP-103 b is metal-rich is controversial, it is all agreed that the atmosphere has a supersolar C/O ratio. It is also notable that both our work and Changeat (2022) detected a large accumulation of H^- and FeH on the dayside of WASP-103 b.

5 SUMMARY

We took two secondary eclipses observations of the HJ WASP-103 b with CFHT/WIRCam in J and K_s, and reanalysed the data observed by Delrez et al. (2018) in K_s band. After correcting the contamination from a faint nearby star, the derived eclipse depths are 0.131 ± 0.022 per cent and 0.135 ± 0.027 per cent in J and K_s, respectively. Our J-band eclipse depth is consistent with Cartier et al. (2016) and Kreidberg et al. (2018) within $1\,\sigma$. The *HST*/WFC3 emission spectra covering 1.15–1.65 μm and *Spitzer*/IRAC broad-band photometry (3.6 and 4.6 μm bands) are combined with our J and K_s measurements to study the atmopshere of WASP103 b.

The retrieval analysis performed in this study assuming equilibrium or free chemistry yield in general similar conclusions that the atmosphere is quite metal rich and carbon rich with respect to its host star and the sun. However, the calculated C/O ratios are quite different, which should be due to two facts. One is that the retrieved T–P profiles are different. The other is that the fractions of each contributing molecules are different, as could be observed in Fig. 9. For example, the carbon-bearing molecules CO and CO_2 in the EQ model are much more prominent than those in the FREE model, while the situation for TiO and VO are on the contrary. This two changes naturally lead to the obviously different C/O ratios between the EQ and FREE models. We note that assuming equilibrium chemistry might not be suitable, as many UHJ appear not at the chemical equilibrium state due to the observed enrichment in refractory elements. On the other side, the use of FREE model could also be risky for some cases as the fractions of individual species could be non-physical. The dayside atmosphere is best fit with a thermal inversion on the dayside, which is likely associated with the strong optical absorber FeH, instead of TiO or VO, given the high temperature in this planet. A large abundance of FeH and H^- is favoured by the free chemistry retrieval, in agreement with the

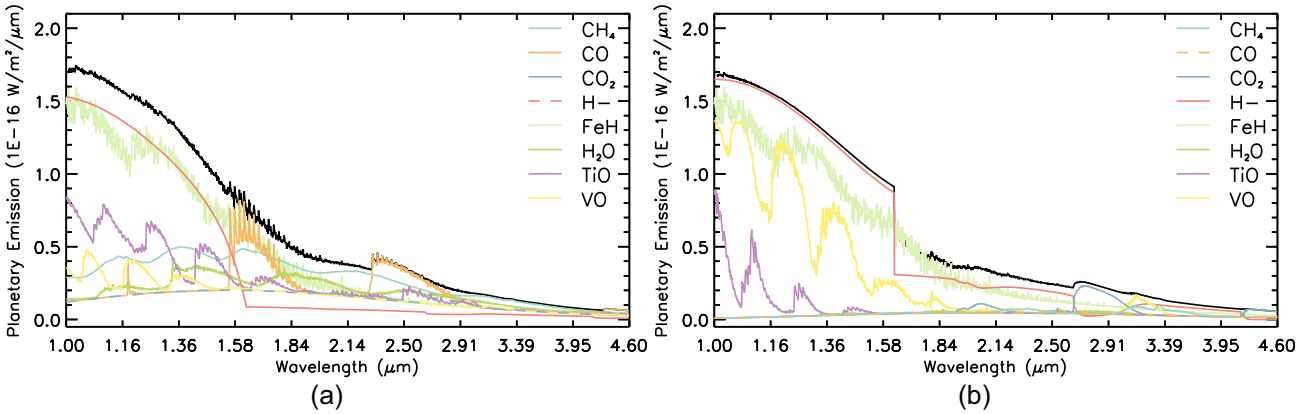

Figure 9. The emission spectra of the most dominant species in our EQ and FREE models. The left-hand panel shows the EQ model, and the right-hand panel shows the FREE model.

Table 4. The Bayesian evidence difference of the model with a certain molecule not included as compared to the full model for the FREE retrievals.

Model	$\Delta\ln(\mathcal{Z})$	Bayes factor
No CO_2	$+4.5 \pm 1.02$	90.02
No H^-	$+3.7 \pm 1.28$	40.45
No CH_4	$+2.8 \pm 1.22$	16.5
No TiO	$+2.1 \pm 1.11$	8.17
No FeH	$+1.9 \pm 1.22$	6.69
No H2O	$+1.0 \pm 1.22$	2.72
No VO	$+0.9 \pm 1.34$	2.45
No CO	-2.4 ± 1.12	0.09

discovery in Changeat (2022). A supersolar C/O ratio (0.86 or 1.5) is recommended by our retrieval analysis, which is consistent with the conclusions from Cartier et al. (2016), Kreidberg et al. (2018), and Changeat (2022). Our analysis suggests that the atmosphere has a supersolar metallicity of ∼2.19 dex, confirming the previous finding by Kreidberg et al. (2018), although Cartier et al. (2016) and Changeat (2022) obtained a solar metallicity. We emphasize here that adding a filter at ∼2.2 μm to the *HST*/WFC3 data may provide crucial information on the chemical compositions, particularly carbon oxides CO_2 and CO. Future emission spectroscopy observations of WASP103 b with *JWST*, for example, are needed to yield more reliable metallicity and C/O ratio measurements, as well as mass fractions of individual atoms/molecules in the atmosphere.

ACKNOWLEDGEMENTS

This research is supported by the National Natural Science Foundation of China grants no. 11988101, 42075123, 42005098, and 62127901, the National Key R&D Program of China No. 2019YFA0405102, the Strategic Priority Research Program of Chinese Academy of Sciences, grant no. XDA15072113, and the China Manned Space Project with NO. CMS-CSST-2021-B12. Y-QS, MZ, and J-SH are supported by the Chinese Academy of Sciences (CAS), through a grant to the CAS South America Center for Astronomy (CASSACA) in Santiago, Chile. The authors thanks the referee for the constructive and useful comments and suggestion. This research uses data obtained through the Telescope Access Program (TAP), which has been funded by the National Astronomical Observatories of China, the Chinese Academy of Sciences (the Strategic Priority Research Program 'The Emergence of Cosmological Structures' Grant No. XDB09000000), and the Special Fund for Astronomy from the from the Ministry of Finance. Two observational nights (2015 May 28 and June 9) with the WIRCam on the 3.6 m CFHT telescope were distributed to us for scientific studies of exoplanetary atmosphere via the TAP. This paper makes use of EXOFAST (Eastman et al. 2013) as provided by the NASA Exoplanet Archive, which is operated by the California Institute of Technology, under contract with the National Aeronautics and Space Administration under the Exoplanet Exploration Program.

DATA AVAILABILITY

The CFHT data are accessible via the Canadian Astronomy Data Centre portal at https://www.cadc-ccda.hia-iha.nrc-cnrc.gc.ca/en/cfht/. The EXOFAST code is accessible following the instruction via https://astroutils.astronomy.osu.edu/exofast/pro/exofast/README. The `petitRADTRANS` retrieval modelling code and associated PYTHON scripts for parameter analysis and plotting are available via https://petitradtrans.readthedocs.io/en/latest/content/installation.html.

REFERENCES

Al-Refaie A. F., Changeat Q., Waldmann I. P., Tinetti G., 2021, ApJ, 917, 37
Alexoudi X. et al., 2018, A&A, 620, A142
Barros S. C. C. et al., 2022, A&A, 657, A52
Barton E. J., Hill C., Yurchenko S. N., Tennyson J., Dudaryonok A. S., Lavrentieva N. N., 2017, J. Quant. Spectrosc. Radiat. Transfer, 187, 453
Barton E. J., Yurchenko S. N., Tennyson J., 2013, MNRAS, 434, 1469
Baudino J.-L., Mollière P., Venot O., Tremblin P., Bézard B., Lagage P.-O., 2017, ApJ, 850, 150
Baxter C. et al., 2020, A&A, 639, A36
Benneke B., Seager S., 2013, ApJ, 778, 153
Borysow A., 2002, A&A, 390, 779
Borysow A., Frommhold L., Moraldi M., 1989, ApJ, 336, 495
Borysow A., Jorgensen U. G., Fu Y., 2001, J. Quant. Spectrosc. Radiat. Transfer, 68, 235
Borysow J., Frommhold L., Birnbaum G., 1988, ApJ, 326, 509
Brogi M., de Kok R. J., Birkby J. L., Schwarz H., Snellen I. A. G., 2014, A&A, 565, A124
Buchner J. et al., 2014, A&A, 564, A125
Burrows A., Budaj J., Hubeny I., 2008, ApJ, 678, 1436
Cartier K. M. et al., 2016, AJ, 153, 34
Cartier K. M. S. et al., 2017, AJ, 153, 34
Casasayas-Barris N., Palle E., Nowak G., Yan F., Nortmann L., Murgas F., 2017, A&A, 608, A135

Chan Y. M., Dalgarno A., 1965, Proc. Phys. Soc., 85, 227
Changeat Q. et al., 2022, ApJS, 260, 3
Changeat Q., 2022, AJ, 163, 106
Croll B. et al., 2015, ApJ, 802, 28
Croll B., Albert L., Lafreniere D., Jayawardhana R., Fortney J. J., 2010a, ApJ, 717, 1084
Croll B., Jayawardhana R., Fortney J. J., Lafrenière D., Albert L., 2010b, ApJ, 718, 920
Dalgarno A., Williams D. A., 1962, ApJ, 136, 690
Dawson R. I., Johnson J. A., 2018, ARA&A, 56, 175
Delrez L. et al., 2018, MNRAS, 474, 2334
Deming D. et al., 2013, ApJ, 774, 95
Deming D., Seager S., 2009, Nature, 462, 301
Devost D., Albert L., Teeple D., Croll B., 2010, in Silva D. R., Peck A. B., Soifer B. T.eds, Proc. SPIE Conf. Ser. Vol. 7737, Observatory Operations: Strategies, Processes, and Systems III. SPIE, Bellingham, p. 77372D
Eastman J., Gaudi B. S., Agol E., 2013, PASP, 125, 83
Edwards B. et al., 2022, preprint (arXiv:2211.00649)
Everett M. E., Howell S. B., 2001, PASP, 113, 1428
Feroz F., Hobson M. P., Bridges M., 2009, MNRAS, 398, 1601
Ford E. B., 2005, AJ, 129, 1706
Fortney J. J., Lodders K., Marley M. S., Freedman R. S., 2008, ApJ, 678, 1419
Gandhi S., Madhusudhan N., 2019, MNRAS, 485, 5817
Gibson N. P., Aigrain S., Barstow J. K., Evans T. M., Fletcher L. N., Irwin P. G. J., 2013, MNRAS, 436, 2974
Gillon M. et al., 2014, A&A, 562, L3
Gray D. F., 2021, The Observation and Analysis of Stellar Photospheres. Cambridge Univ. Press, Cambridge
Harris G. J., Tennyson J., Kaminsky B. M., Pavlenko Y. V., Jones H. R. A., 2006, MNRAS, 367, 400
John T. L., 1988, A&A, 193, 189
Kass R. E., Raftery A. E., 1995, J. Am. Stat. Assoc., 90, 773
Kawashima Y., Min M., 2021, A&A, 656, A90
Kirk J. et al., 2021, AJ, 162, 34
Knutson H., 2009, American Astronomical Society Meeting Abstracts, #201.06
Kreidberg L. et al., 2018, AJ, 156, 17
Kreidberg L. et al., 2022, AJ, 164, 124
Lendl M., Cubillos P. E., Hagelberg J., Müller A., Juvan I., Fossati L., 2017, A&A, 606, A18
Lothringer J. D., Barman T., 2019, ApJ, 876, 69
Mackebrandt F. et al., 2017, A&A, 608, A26
Madhusudhan N. et al., 2011a, Nature, 469, 64
Madhusudhan N., Agúndez M., Moses J. I., Hu Y., 2016, Space Sci. Rev., 205, 285
Madhusudhan N., Mousis O., Johnson T. V., Lunine J. I., 2011b, ApJ, 743, 191
Madhusudhan N., Seager S., 2009, ApJ, 707, 24
Madhusudhan N., Seager S., 2011, ApJ, 729, 41
Mandel K., Agol E., 2002, ApJ, 580, L171
Mansfield M. et al., 2021, Nat. Astron., 5, 1224
Mansfield M. et al., 2022, AJ, 163, 261
McGruder C. D. et al., 2022, AJ, 164, 134
McKemmish L. K., Masseron T., Hoeijmakers H. J., Pérez-Mesa V., Grimm S. L., Yurchenko S. N., Tennyson J., 2019, MNRAS, 488, 2836
Mollière P., van Boekel R., Bouwman J., Henning T., Lagage P. O., Min M., 2017, A&A, 600, A10
Mollière P., Wardenier J. P., van Boekel R., Henning T., Molaverdikhani K., Snellen I. A. G., 2019, A&A, 627, A67
Murgas F., Chen G., Nortmann L., Palle E., Nowak G., 2020, A&A, 641, A158
Ngo H. et al., 2016, ApJ, 827, 8
Nikolov N. et al., 2014, MNRAS, 437, 46
Pass E. K., Cowan N. B., Cubillos P. E., Sklar J. G., 2019, MNRAS, 489, 941
Piskunov N. E., Kupka F., Ryabchikova T. A., Weiss W. W., Jeffery C. S., 1995, A&AS, 112, 525
Puget P. et al., 2004, in Moorwood A. F. M., Iye M.eds, Proc. SPIE Conf. Ser. Vol. 5492, Ground-Based Instrumentation for Astronomy. SPIE, Bellingham, p. 978
Rothman L. S. et al., 2010, J. Quant. Spectrosc. Radiat. Transfer, 111, 2139
Rothman L. S. et al., 2013, J. Quant. Spectrosc. Radiat. Transfer, 130, 4
Roudier G. M., Swain M. R., Gudipati M. S., West R. A., Estrela R., Zellem R. T., 2021, AJ, 162, 37
Seager S., Deming D., 2010, ARA&A, 48, 631
Sing D. K. et al., 2016, Nature, 529, 59
Sousa-Silva C., Al-Refaie A. F., Tennyson J., Yurchenko S. N., 2015, MNRAS, 446, 2337
Southworth J. et al., 2015, MNRAS, 447, 711
Southworth J., Evans D. F., 2016, MNRAS, 463, 37
Stevenson K. B. et al., 2010, Nature, 464, 1161
Wang W., van Boekel R., Madhusudhan N., Chen G., Zhao G., Henning T., 2013, ApJ, 770, 70
Welbanks L., Madhusudhan N., Allard N. F., Hubeny I., Spiegelman F., Leininger T., 2019, ApJ, 887, L20
Wende S., Reiners A., Seifahrt A., Bernath P. F., 2010, A&A, 523, A58
Wilson J. et al., 2020, MNRAS, 497, 5155
Winn J. N. et al., 2008, ApJ, 683, 1076
Wöllert M., Brandner W., 2015, A&A, 579, A129
Yan F. et al., 2022, A&A, 659, A7
Yip K. H., Changeat Q., Edwards B., Morvan M., Chubb K. L., Tsiaras A., Waldmann I. P., Tinetti G., 2021, AJ, 161, 4
Yurchenko S. N., Barber R. J., Tennyson J., 2011, MNRAS, 413, 1828
Yurchenko S. N., Tennyson J., 2014, MNRAS, 440, 1649

APPENDIX A: ADDITIONAL FIGURES

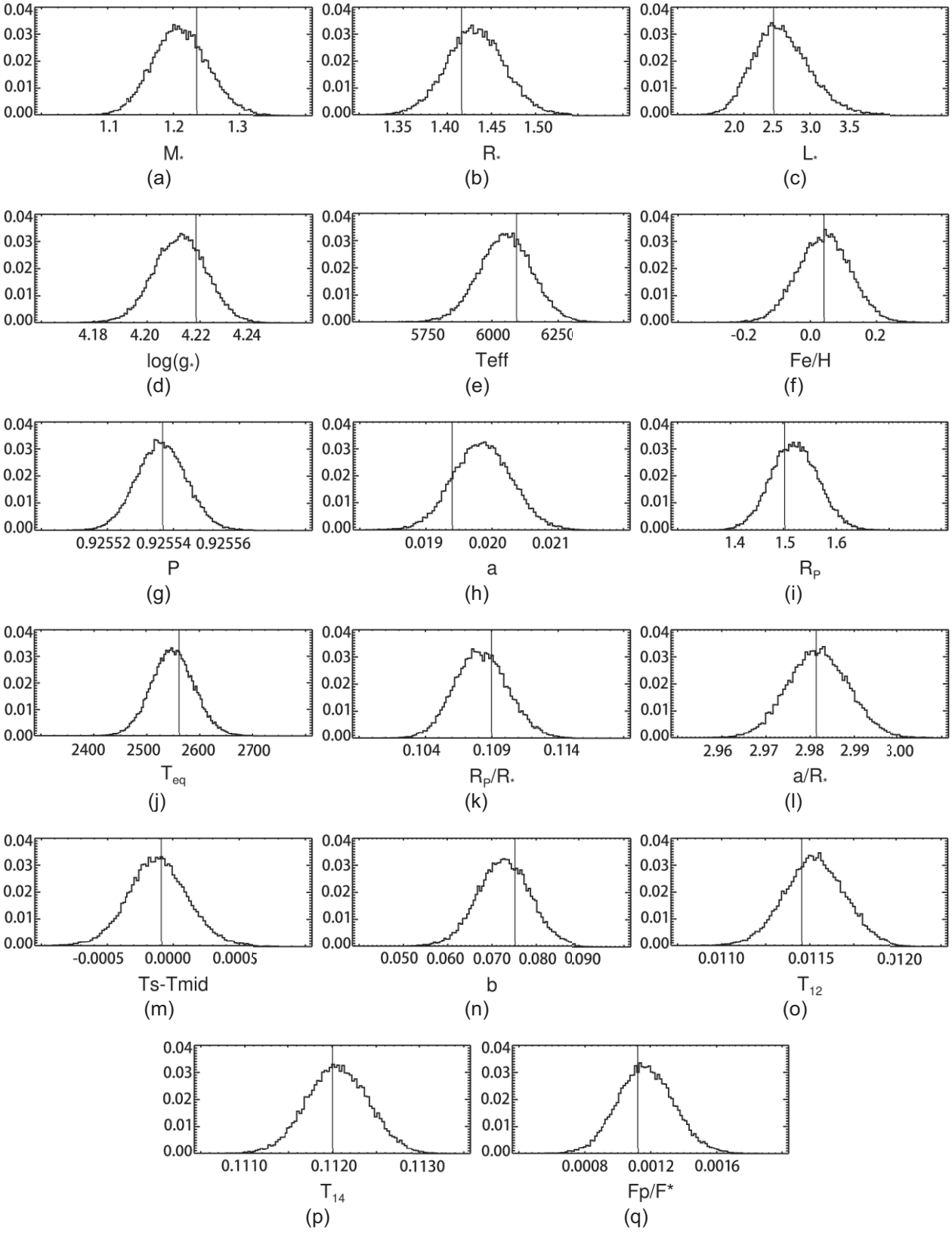

Figure A1. The distribution plots of the EXOFAST fitting parameters in *J* band.The *y*-axis represents probability.

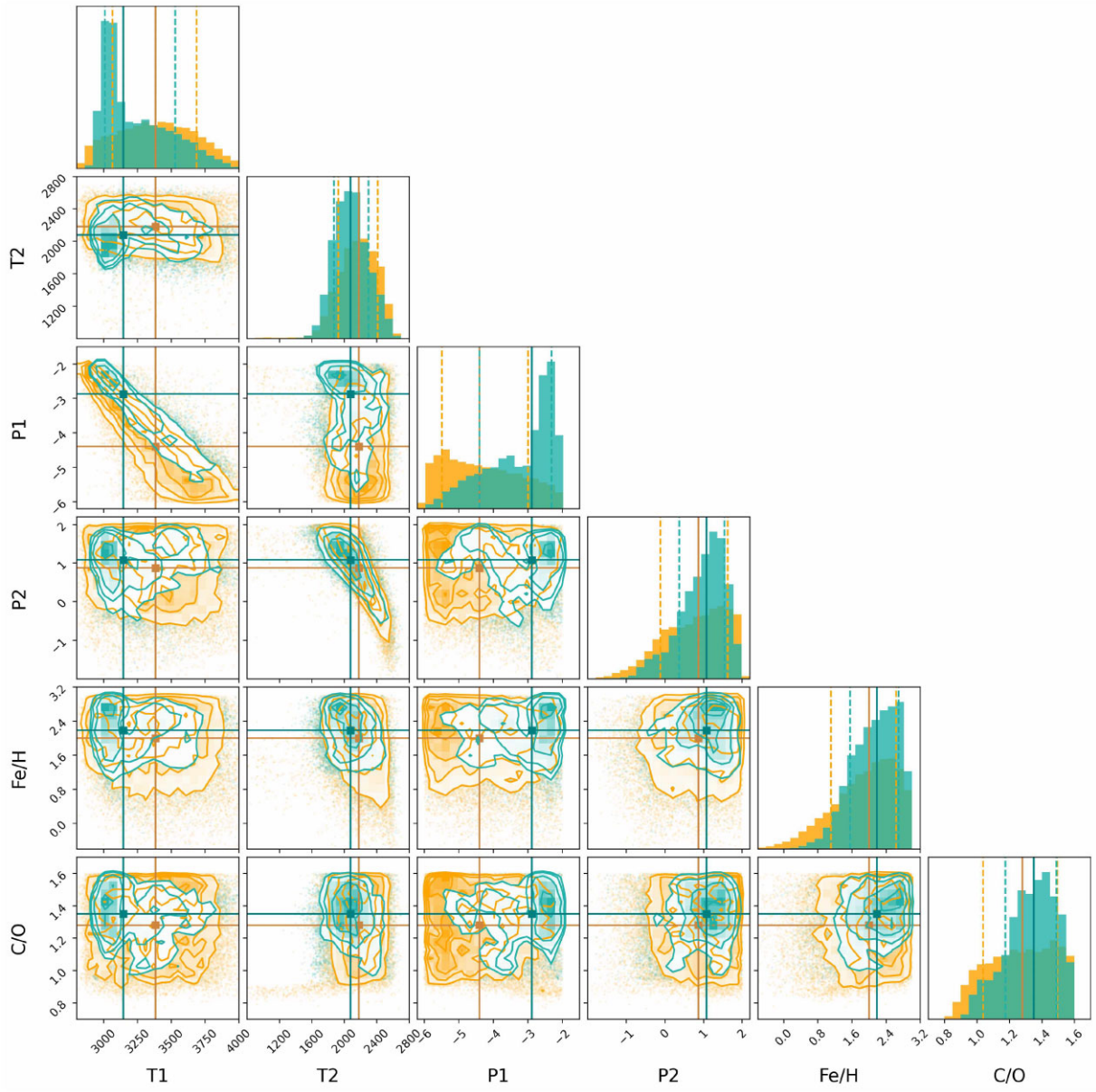

Figure A2. The retrieved atmospheric properties for the EQ retrievals on the unoffset data (green) and the 'os $= -200$' data (yellow) with `petitRADTRANS`. The panels show the posterior distribution of parameters from the nested sampling run. Darker shading corresponds to higher posterior probability. The diagonal shows a one-dimensional histogram for each parameter, with dotted lines denoting the median and 1σ credible interval. The solid lines indicates the maximum likelihood estimation value.

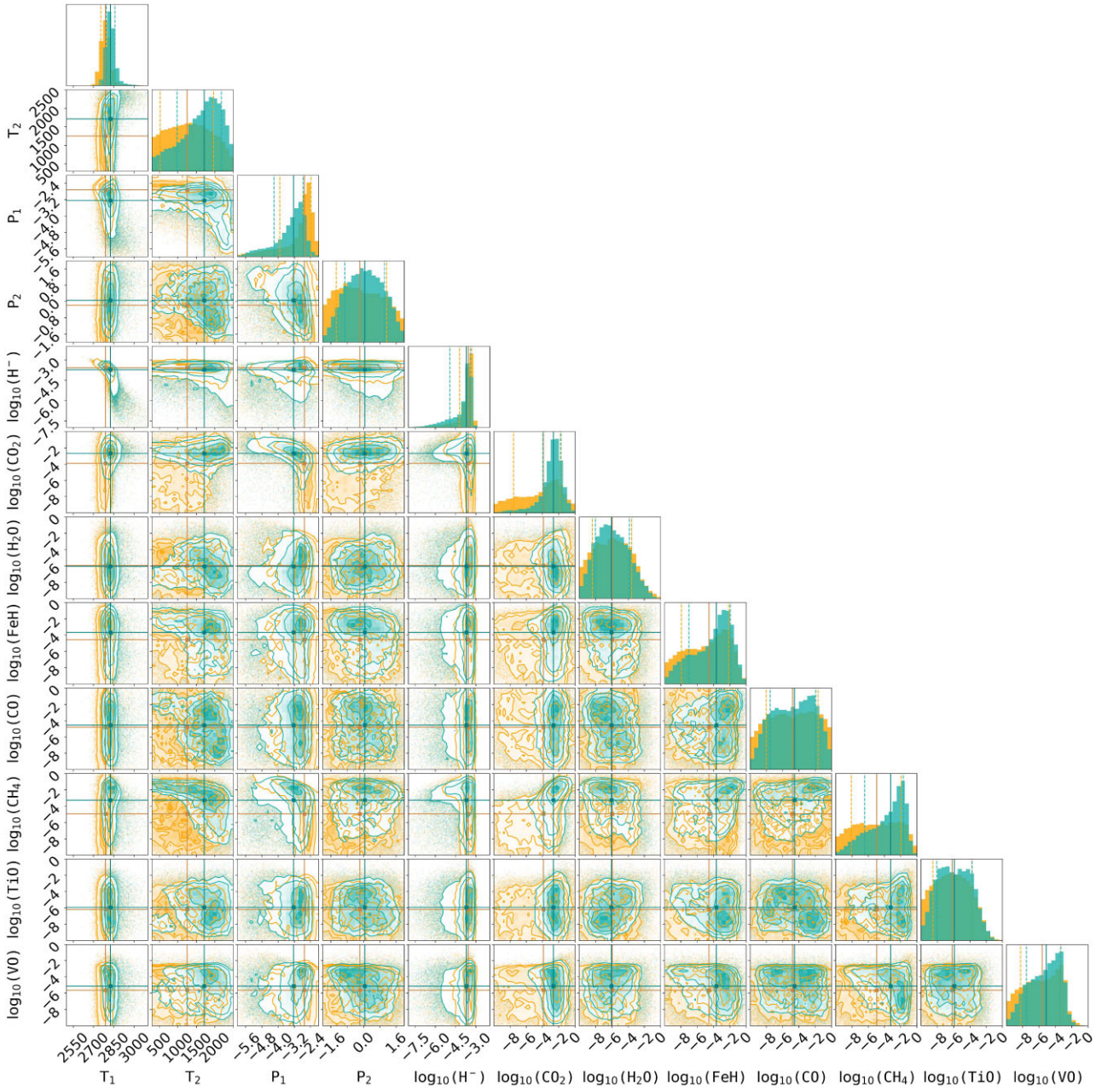

Figure A3. The retrieved atmospheric properties for the FREE retrieval on the unoffset data (green) and the 'os = −50' data (yellow) with `petitRADTRANS`. The orange corners represent the FREE retrieval after applying an offset of −50 ppm to the *HST* data.

This paper has been typeset from a TEX/LATEX file prepared by the author.